

Supporting Information

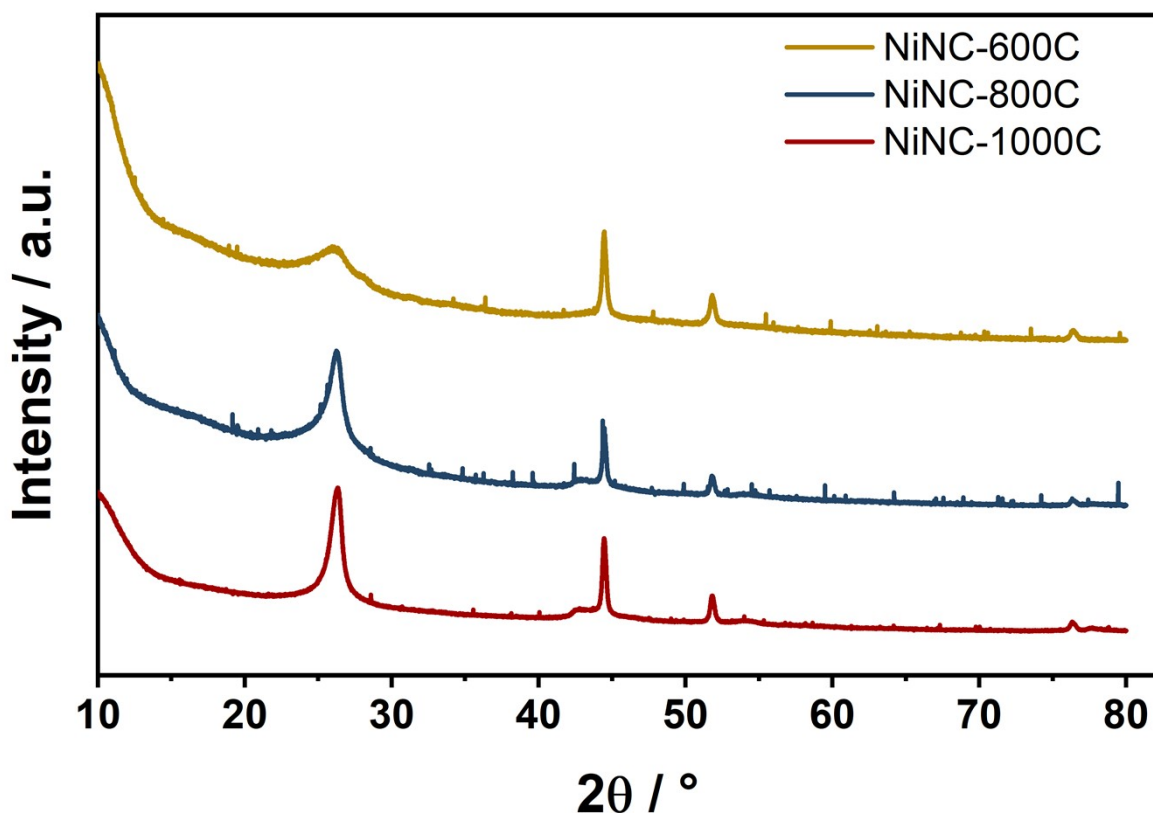
1. Catalyst synthesis

Zeolitic Imidazole Frameworks (ZIF) were synthesized by a wet chemical method reported previously. Specifically, 5.3 g of 2-methylimidazole were dissolved in 100 mL of methanol, forming **solution A**; nickel chloride was dissolved in 100 mL methanol forming a 2% mixture (**solution B**). Subsequently, **solution B** was slowly added into **solution A**, and the obtained mixture was then kept at room temperature for 24 h. During this process, vigorous magnetic stirring was kept. Afterwards, the formed precipitate was collected by centrifuge, washed 3 times with methanol, and then dried in vacuum at 60 °C. The dry powders were subsequently calcined in a tube furnace at 550 °C for 1 h, and afterwards at an elevated temperature of 600 °C, 800 °C, and 1000 °C for another 1 h. During the whole calcination process, high-purity nitrogen (99.999%) flowed through the quartz tube at a rate of 100 sccm. The furnace was then cooled down to room temperature. Finally, the obtained NiNC powders were chemically etched in concentrated HNO₃ at 80 °C for 5 h to remove metallic nickel left on the surface.

Nickel nitrides with various Ni:N ratios were prepared in several different ways. 1) “Ni₃N” preparation. We perform nitridation of nickel via implantation of pure Ni by nitrogen ions.(1) The Ni foil was sputter-etched with 5 keV argon beam to remove all O and C contaminations prior to in-situ nitridation. The nitridation of the foils was performed via ion implantation of nitrogen ions by means of a SPECS IQE11/35 (SPECS) ion source operated at 1 keV under an N₂ partial pressure of 10⁻⁵ mbar. The nitrogen implantation was continued until saturation of the N/Ni ratio in the XPS spectra. The implantation dose was estimated as ~10¹⁶ ions/cm². The nickel nitride sample prepared via nitrogen ion implantation will be referred to as “Ni₃N”.

The Ni(II) Phtalocyanine (Ni(II)Pc) and Ni(II) Porphyrin films (Ni(II)TPP) were grown via thermal evaporation of the corresponding powder on a freshly cleaved HOPG and gold coated silicon wafer respectively in the sample preparation chamber of the XPS spectrometer by following the procedures described by Petraki et al.(2) for Ni(II)Pc and Dongol et al(3) for (Ni(II)TPP). The substrates were kept at room temperature during the deposition. The thicknesses of the films were made large enough to be detected by visual observation of characteristic coloration of the surface.

2. Characterisation

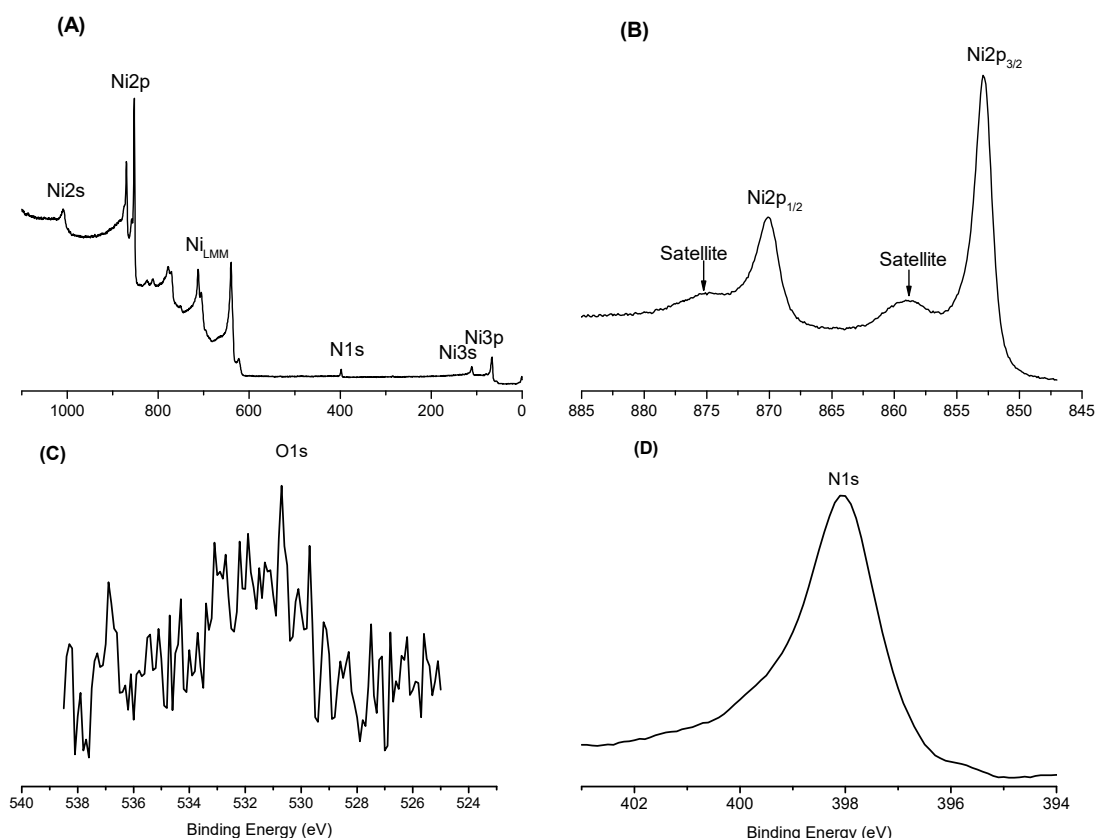


Supplementary Figure 1: XRD of the NiNC catalyst at different pyrolysis temperatures.

3. Supplementary Note 1

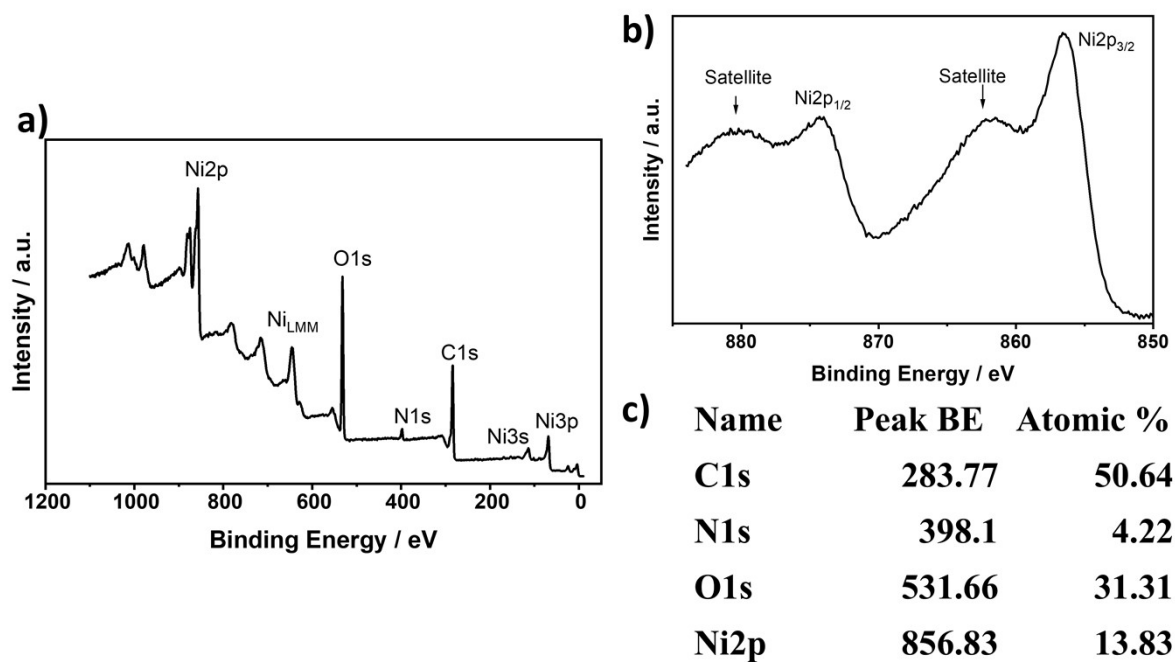
In *Supplementary Figure 2* we present XPS spectra from the “Ni₃N” sample prepared via nitrogen implantation into the pure Ni foil. The survey XPS spectrum, *Supplementary Figure 2a*, evidences the formation of pure, adventitious carbon free, surface layer of nickel nitride. *Supplementary Figure 2b* depicts Ni2p spectrum with two peaks due to spin-orbit splitting and two satellite peaks. The main peak at 852.6 eV corresponds to Ni2p_{3/2}. The satellite peak ~6 eV away to the higher binding energies from the main peak was fitted with the Lorentzian-Gaussian curve and its intensity accounts for 16% of that for the main peak. The position of the N1s peak, shown in *Supplementary Figure 2d*, is 398 eV. The peak position and the peak shape are similar to those reported for transition metal nitrides,⁽⁴⁻⁷⁾ where nitrogen is in 3⁻ oxidation state. The quantitatively estimated atomic concentration Ni-to-N ratio was found to be close to 3:1, and therefore this sample is considered the Ni₃N compound. Nickel is the last element of the 3d metals that forms interstitial nitrides. Ni₃N has an octahedral coordination of interstitial N atoms⁽⁸⁾ with 1⁺ formal oxidation state of nickel. The O1s XPS spectrum, acquired with long accumulation, reveals traces of oxygen (*Supplementary Figure 2c*). But the O1s peak position

at ~532 eV is characteristic of some surface contamination, not of the metal oxide (529-531 eV).



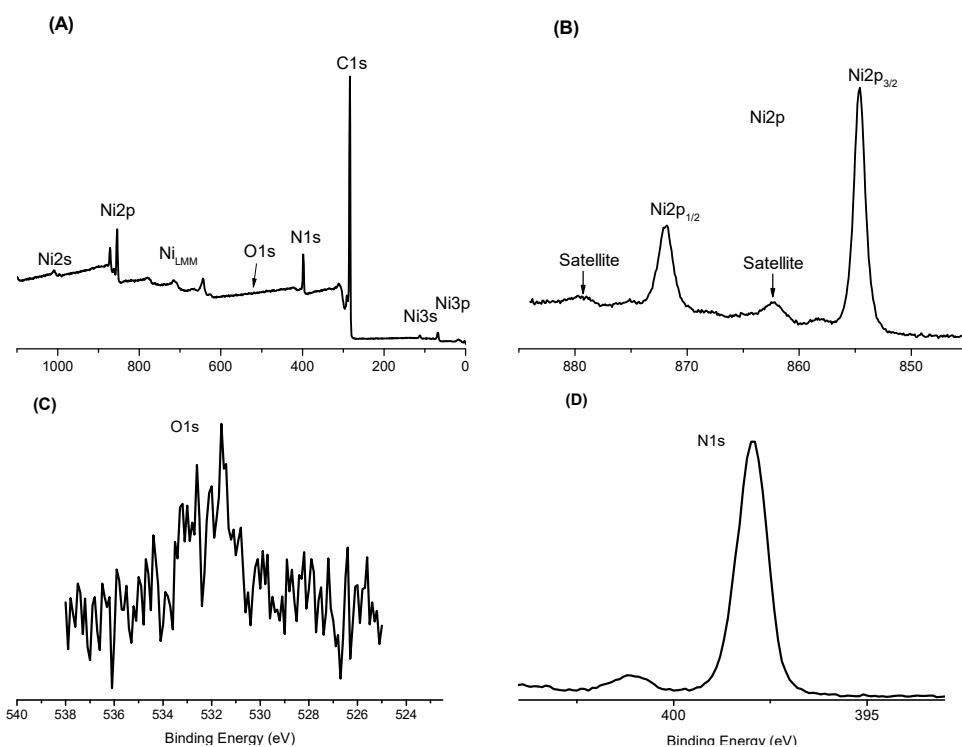
Supplementary Figure 2: XPS spectra of the “Ni₃N” surface layer prepared via nitrogen ion implantation. Ni to N ratio is ~3:1. Intensity ratio Ni2p_{3/2} satellite to Ni2p_{3/2} main peak is 0.16.

To shed some light on the electronic and atomic structure of the NiNC-1000C sample and given the Ni-to-N ratio is close to 4 we turned to Ni porphyrin (Ni TPP powder), which has a planar structure with, ideally, 4 nitrogen atoms around one nickel atom. So, one should expect N-to-Ni ratio determined by the XPS also close to 4. The XPS spectra of Ni(II) TPP powder (**Supplementary Figure 3**) reveal strong surface oxidation with formation of NiO_x compounds.



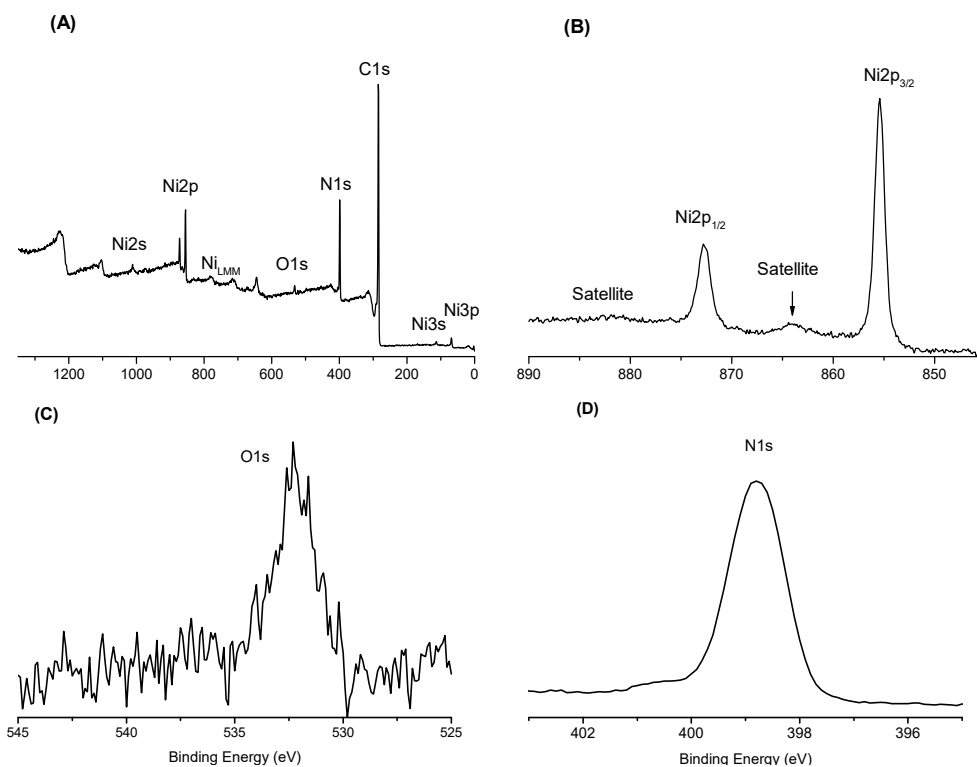
Supplementary Figure 3: XPS spectra from Nickel(II) 5,10,15,20-(Tetraphenyl)Porphyrin (Ni-TPP powder) as loaded. Ni2p spectrum indicates strong oxidation of Ni.

It could be a mixture of NiO, Ni(OH)₂, and NiOOH. Therefore, we tried to prepare Ni TPP films via thermal deposition in the XPS chamber. The Ni TPP films were grown on a gold coated Si wafer and the XPS spectra, shown in *Supplementary Figure 4*, were acquired after deposition without exposure to the ambient atmosphere.



Supplementary Figure 4: XPS spectra of Ni TPP film. Ni to N ratio is $\approx 1:4$. Intensity ratio Ni2p_{3/2} satellite to Ni2p_{3/2} main peak is 0.14.

Similar experiments were performed with Ni(II) Phtalocyanine powder. The Ni(II) Phtalocyanine has also planar structure with Ni in the same oxidation state 2⁺ but the N-to Ni ratio is 8, twice as big as in Ni(II) TPP powder. The XPS spectra for Ni Pc film in-situ deposited on the graphite substrate are presented in *Supplementary Figure 5*.



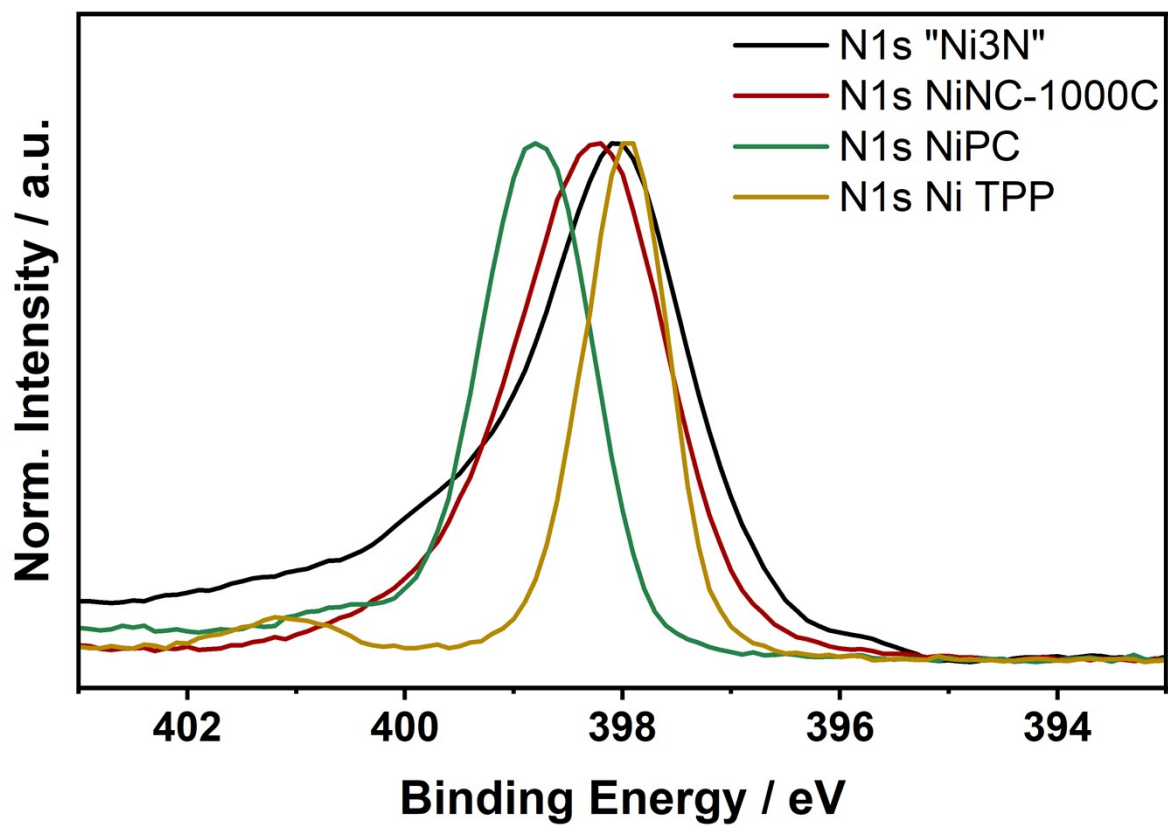
Supplementary Figure 5: XPS spectra of Ni(II)Pc film evaporated in-situ on graphite. Ni to N ratio is $\approx 1:7$. Intensity ratio Ni2p_{3/2} satellite to Ni2p_{3/2} main peak is 0.14.

Supplementary Table 1 lists the positions of Ni2p_{3/2} main peaks, apparent chemical shifts (ΔE_b), and N:Ni ratio for various nickel nitrides in comparison to nickel oxides. It is noteworthy that the chemical shift of Ni 2p level in the Ni(II) TPP film is quite different from that in Ni(II) Pc film despite the fact that Ni is in the same oxidation state 2⁺ for both materials. Even more, chemical shift in the studied nitrides follows the trend: Ni₃N < NiNC-1000C < Ni(II) TPP film < Ni(II) Pc film. Thus, it appears reasonable to conclude that the formal oxidation state of Ni in the NiNC-1000C compound is between 1⁺ and 2⁺. Overall, chemical shift of the XPS peaks depends on the charge screening mechanisms of the core holes created during photoelectron emission – so called initial and final state effects. It is obvious from the data presented above that the initial and final state effects in Ni are quite different in the studied nickel nitrides even when nickel is in the same oxidation state 2⁺ or close to it.

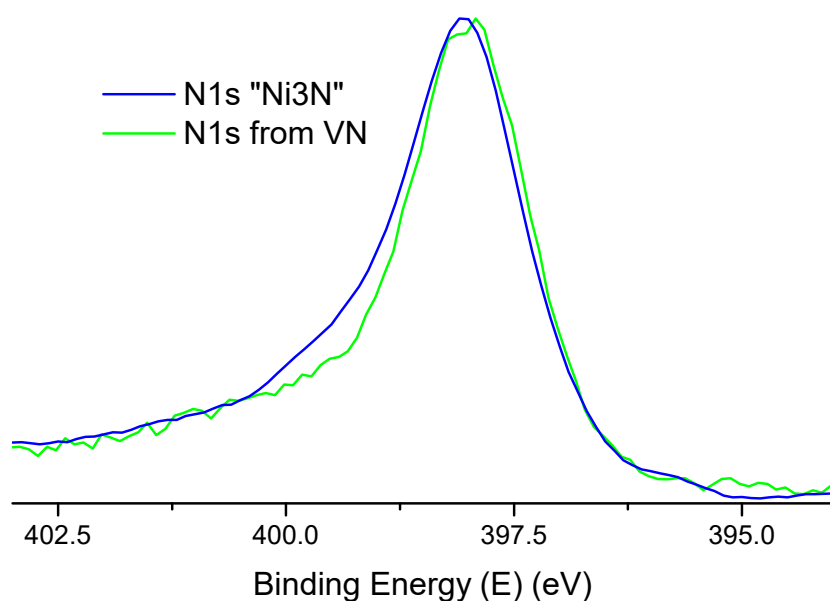
*Supplementary Table 1: Further XPS analysis results. Ni2p_{3/2} peak maximum positions for various Ni based compounds with oxidation state of Ni ranging from 0 to 3+. *Ni oxidation state determined in this study.*

	Formal oxidation state	N:Ni	Ni2p _{3/2} peak maximum, eV
Ni metal	0	-	852.5
Ni ₃ N	1+	1:3.1	852.6
NiO	2+	-	853.6
NiNC-1000C*	2+	3.75:1	854.6
Ni TPP	2+	3.4:1	854.9
Ni Pc	2+	7:1	855.44
Ni(OH) ₂₍₉₎	2+	-	855.8
γ-NiOOH(9)	3+	-	855.8

Comparison NiNC-1000C, Ni Pc and Ni TPP. Structural differences between NiNC-1000C and Ni Pc also based on the comparison of Ni/N atomic concentration ratios. Indeed, for Ni Pc the ratio 1:7, which is close to the ideal 1:8 dictated by the structural form of the Ni(II) Phthalocyanine molecule. In contrast, for NiNC-1000C the ratio is 1:3.75 \approx 4, thus revealing 2 times less of N atoms surrounding Ni atom. The Ni (II) porphyrine molecule has also planar structure with N:Ni = 4:1. Comparison of the XPS spectra from the NiNC-1000C sample and Ni TPP film shows rather small difference (0.3 eV) in the main peak position. But it is substantially bigger for the Ni Pc film -1 eV. Overall, the common feature observed in the Ni2p spectra for NiNC-1000C, Ni TPP, and Ni Pc is the small intensity of the shake-up satellite, which is in a drastic contrast to the nickel compounds containing oxygen. We speculate that electronically NiNC-1000C should be similar to the Ni TPP. Noteworthy, the width of the N1s spectral line of the NiNC-1000C sample, shown in **Supplementary Figure 6**, is apparently much larger than that of Ni TPP and Ni Pc films. That most probably points to the structural differences between NiNC-1000C and Ni TPP compounds. Addressing this issue is beyond the scope of this paper.



Supplementary Figure 6: N1s XPS spectra from NiNC-1000C (via ZIF synthesis) in comparison with the N1s from "Ni3N", Ni TPP film and Ni Pc film evaporated in vacuum. Each spectrum was normalized to its maximum intensity.



Supplementary Figure 7: N1s spectra from “Ni₃N” (prepared via N₂⁺ implantation) in comparison with N1s from oxygen free VN film.(4)

Supplementary Table 2: ICP-OES and elemental analysis of the NiNC catalyst at different pyrolysis temperature.

	ICP	EA				Total
	Ni (%)	C (%)	O (%)	N (%)	H (%)	
NiNC- 600C	11.9	69.2	8.39	7.20	1.06	97.75
NiNC-800C	11.3	70.5	8.9	4.83	0.97	96.5
NiNC-1000C	5.05	90	2.9	2.16	0.51	100.62

Supplementary Table 3: **BET analysis of the NiNC catalyst at different pyrolysis temperature.**

BET	S_{BET} (m^2g^{-1})	V_{micro} (cm^3g^{-1})	S_{meso} (m^2g^{-1})	V_{pore} (cm^3g^{-1})
NiNC-600C	148	0	148	0.29
NiNC-800C	327	0.03	269	0.43
NiNC-1000C	234	0	234	0.44

4. Full-Cell measurements and fabrication of the applied electrodes for CO₂RR.

4.1 Cathode fabrication for CO₂RR

40 mg NiNC catalyst, 60 mg PTFE powder (Sigma Aldrich, 1 μm particle size), 2 mL ethanol were mixed and sonificated using sonifier horn for 15 mins. The prepared ink was sprayed coated onto the commercial gas diffusion layer from DeNora (GDL2), on the micro porous layer, at 80 °C.

4.2 BPM Zero-Gap MEA cell assembly

The cathode (5 cm^2), membrane (Fumasep FBM BPM, Fuma Tech, >5 cm^2), and the anode (5 cm^2 , *NiFe(-Cl)-LDH* electrodes) are layer by layer assembled in the electrolyzer. Both cathode and anode are located in a 5 cm^2 window of the sealing PTFE gaskets (thickness: 120 or 800 microns, respectively). After that, the assembly is compressed within the flow field integrated current collectors.

The catholyte-free zero-gap cell was fed with humidified CO₂ which is controlled by a mass flow meter (MFC, Bronkhorst; flow rate 20 ml min^{-1}). After the reactor, the product stream is purged through a condenser (water cooled at RT) and drier (tube filled with molsieve), then mixed with N₂ (5 ml min^{-1}) for GC analysis. At the anode, 1M KOH solution is recycled with 20 mL min^{-1} .

All CO₂RR measurements in this report are done at ambient temperature and pressure. The anode and cathode are connected with a potentiostat (Bio-Logic SP150 with a booster channel) to control the current densities and the reference electrode accompanies the anode for a two-electrodes configuration, and Potentio- electrochemical impedance spectra (PEIS modules) are carried out to measure the cell-resistance. The CO₂RR performance is assessed at various current densities or at one constant current density. Each current step is held for 15 min before moving on to the next current setting, and the gas stream is injected in the GC sample loop at 14.5 min of each current step. If we use one constant current density then we analyze the product stream every 15 min.

When driving the CO₂RR in the flow cell, especially at large current densities or over longer time, significant (bi-)carbonate precipitation should be considered, which causes obvious feed

blockage. Therefore, the N₂ bleeding line implemented in our setup with a defined flow rate (5 mL min⁻¹) serves as an internal standard flow rate.

4.3 Product analysis for CO₂RR Zero-Gap Measurement

A Shimadzu 2014 on-line GC is utilized for product quantification. The gas stream is separated by the Hayesep Q + R columns and then analyzed by the TCD (Thermo Conductivity Detector) and FID (Flame Ionization Detector). The TCD detects the volume percentage (%VOL) of the H₂ product, and the FID measures the CO after being methanized. In all tests, no liquid product is found after the electrolysis.

We use a N₂ bleeding after the reactor and in front of the GC and use the N₂ signal as in-line calibration. The actual total gas flow rate into the GC sample loop could be calculated as **EQ. 1** and can be used to calculate FE, -j_{CO}, etc.

$$\text{EQ. 1} \quad V_{Total} = V_{N_2} + V_{reactor} = \frac{V_{N_2}}{C_{N_2}}$$

V_{Total} :	total stream flow rate in GC	/mL s ⁻¹
V_{N_2} :	defined N ₂ bleeding flow rate	/mL s ⁻¹
$V_{reactor}$:	reactor product stream flow rate	/mL s ⁻¹
C_{N_2} :	N ₂ concentration detected by GC	/%VOL

Calculations of the production rate (**EQ. 2**), partial current density (**EQ. 3**), and faradaic efficiency (**EQ. 4**) are given below.

$$\text{EQ. 2} \quad \dot{n}_{Product} = \frac{V_{Total} \times C_{Product}}{A \times V_{MOL}}$$

$\dot{n}_{Product}$:	geometric reaction rate of each product	/mol cm ⁻² s ⁻¹
-----------------------	---	---------------------------------------

$C_{Product}$:	product concentration (volumetric ratio) from GC	/ %VOL
A :	geometric area of the electrode	/cm ²
V_{MOL} :	volume of gas per mole at atm	/mL
	mol ⁻¹	

EQ. 3
$$j_{Product} = \dot{n}_{Product} \times F \times z$$

$j_{Product}$:	partial current density of each product	/mA
	cm ⁻²	
F :	faradaic constant	/ C mol ⁻¹
z :	charge transfer per product molecule	

EQ. 4
$$FE_{Product} = \frac{j_{Product}}{j_{Total}} \times 100\%$$

$FE_{Product}$:	faradaic efficiency of each product	/ %
j_{Total} :	total current density	/ mA cm ⁻²

To gain more information about the CO₂ consumption we calculate the carbon crossover coefficient from **EQ. 5**.

EQ. 5
$$CCC = \frac{V_{H_2} + V_{CO_2, in} - V_{out}}{V_{CO} + V_{H_2}}$$

V_{H_2} :	volumetric hydrogen flow out of the cell	/mL
	s ⁻¹	

V_{CO} : volumetric carbon monoxide flow out of the cell /mL
s⁻¹

$V_{CO_2,in}$: volumetric carbon dioxide flow in the cell /mL s⁻¹

V_{out} : volumetric total outlet flow /mL s⁻¹

The single pass conversion towards CO is calculate according **EQ. 6**.

EQ. 6

$$SP = \frac{V_{CO}}{V_{CO_2,in}} \times 100$$

The lambda value (**EQ. 7**) is the ratio between CO₂ inlet feed and the non-electrochemical plus electrochemical consumed CO₂ and given by:

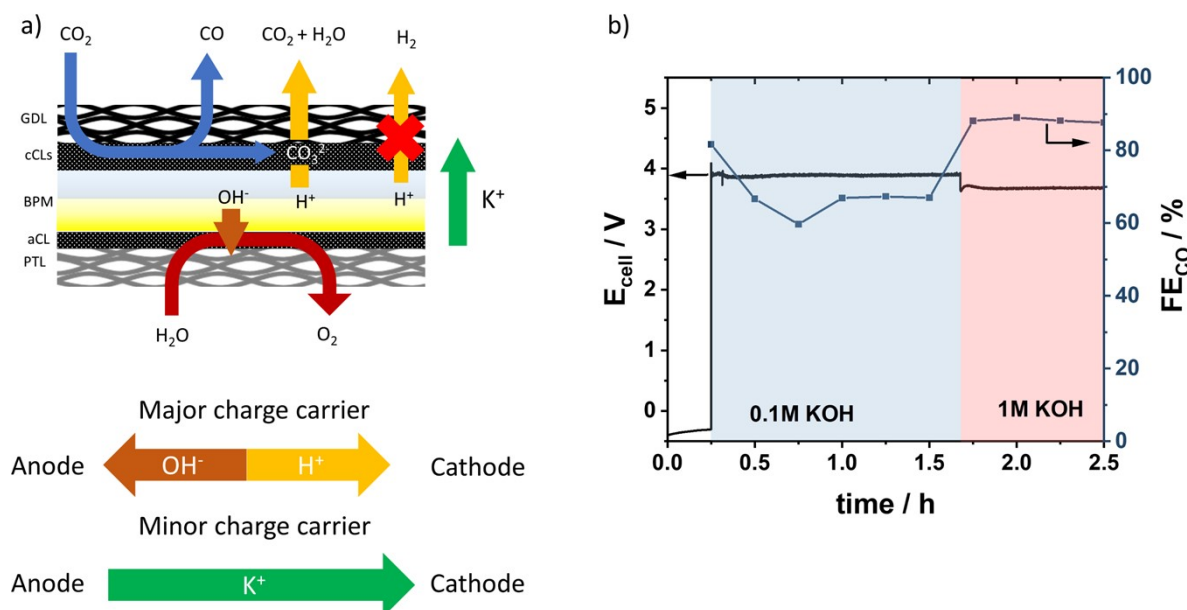
EQ. 7

$$\lambda_{stoich} = \frac{V_{CO_2,in}}{CCC (V_{CO} + V_{H_2}) + V_{CO}}$$

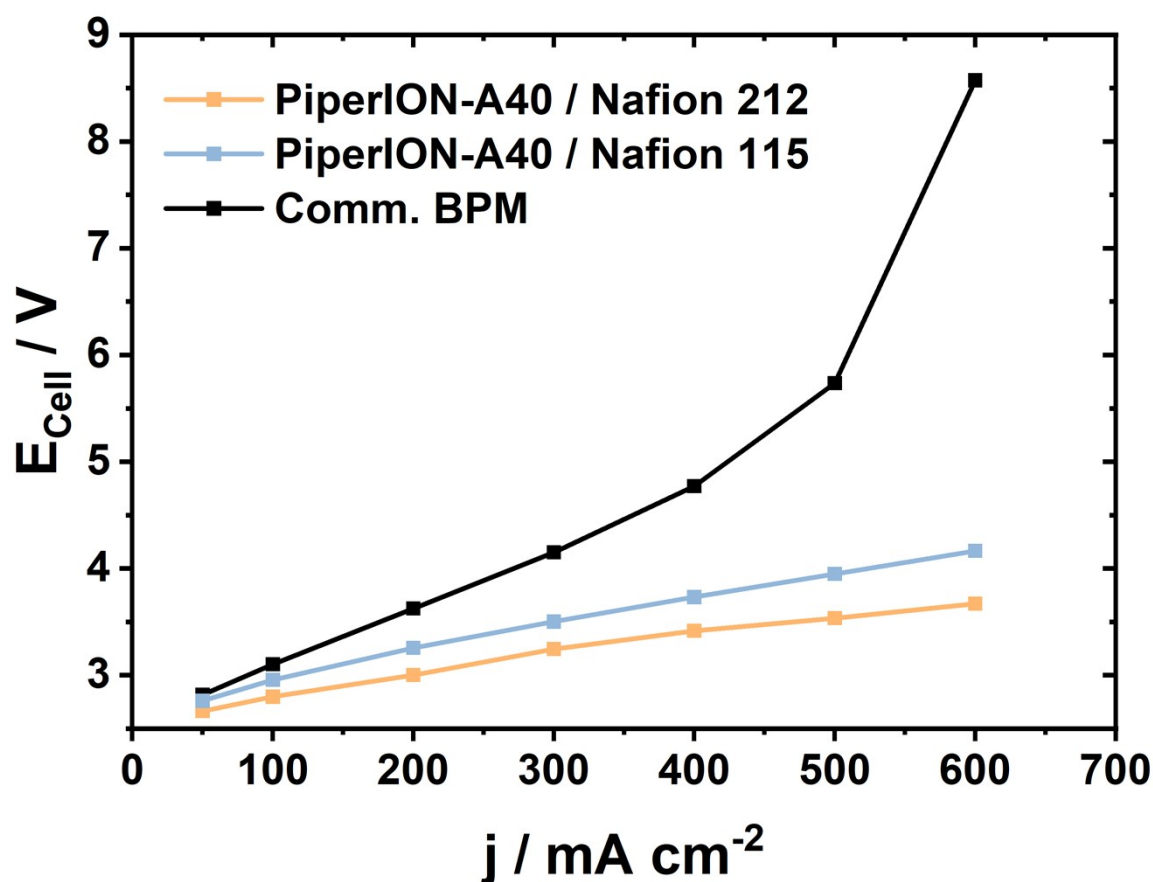
An important information for downstream processes is the CO outlet ratio (**EQ. 8**) and can be calculated as followed:

EQ. 8

$$CO_{outlet} = \frac{V_{CO}}{V_{out} - V_{N_2}} \times 100$$



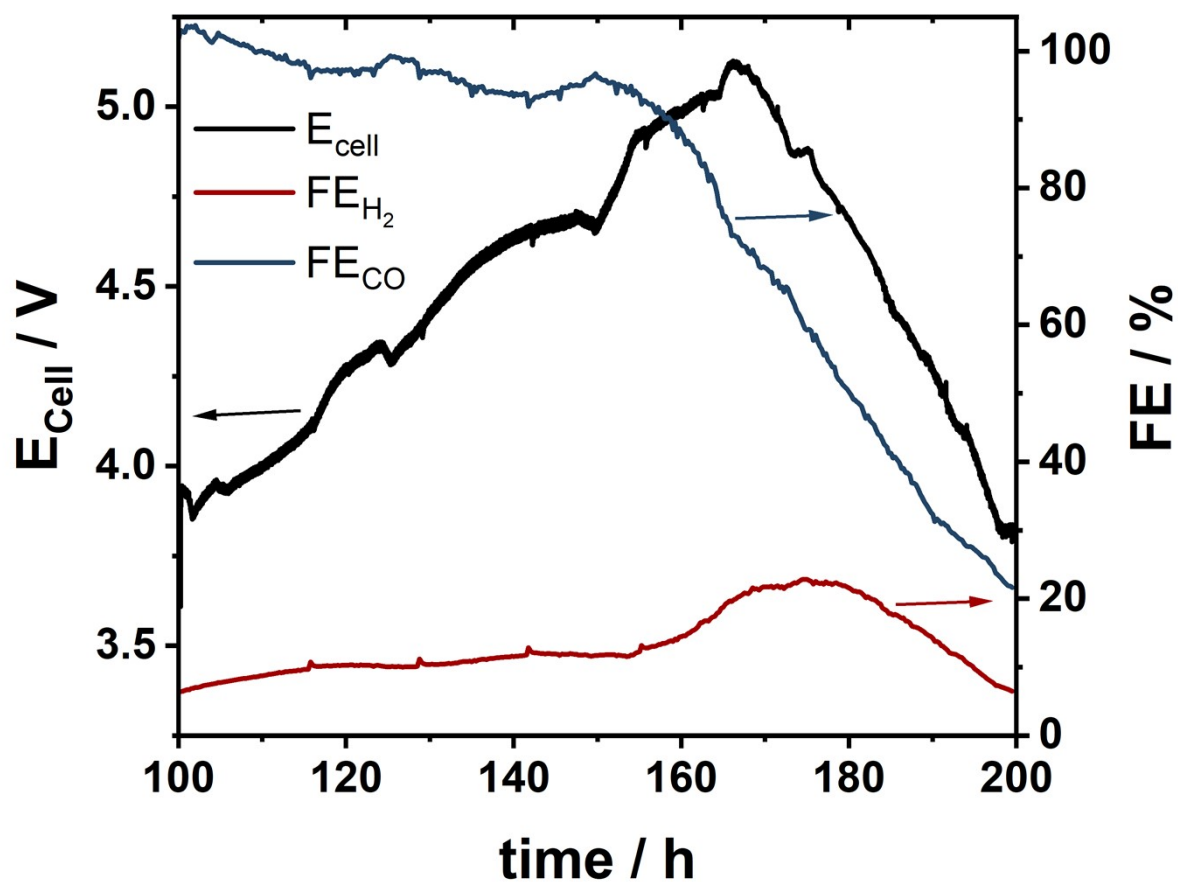
Supplementary Figure 8: **Cation impact in the BPM configuration.** a) Scheme of a BPM MEA with either cathode and anode processes, ion movements and proposed major and minor charge carriers. b) Anolyte cation concentration impact on the selectivity of the cathode.



Supplementary Figure 9: **Self-made bipolar membrane activity.** Polarization curve of different BPMs. PiperION-A40- HCO_3^- (TP-85, 40 μm , Versogen) as anion exchange membrane, activated in 1 M KOH. Nafion membranes are activated in water.

Supplementary Table 4: Comparison to the Literature.

Reference	Potential	Current density	FE _{CO}
This Paper – Commercial BPM	6.5 V	500 mA cm ⁻²	83 %
This Paper – Homemade BPM	3.5 V	500 mA cm ⁻²	77%
Mengran Li et. al.(10)	~4 V	300 mA cm ⁻²	~40 %
Zhifei Yan et. al.(11)	-2.6 V (vs. Ag/AgCl)	~28 mA cm ⁻²	~40 %
Kailun Yang et. al. (12)	~2.8 V	200 mA cm ⁻²	~70 %
Marijn A. Blommaert et. al.(13)	4.7 V	300 mA cm ⁻²	11 %
David M. Weekes et. al.(14)	3.4 V	100 mA cm ⁻²	65 %
Jiyun Kwen et. al.(15)	~3.2 V	100 mA cm ⁻²	~85 %
Bhavin Siritanaratkul et al.(16)	-	100 mA cm ⁻²	66%



Supplementary Figure 10: Extended stability test at 200 mA cm⁻². Extended stability test after 100 h at 100 mA cm⁻² without renewing the anolyte.



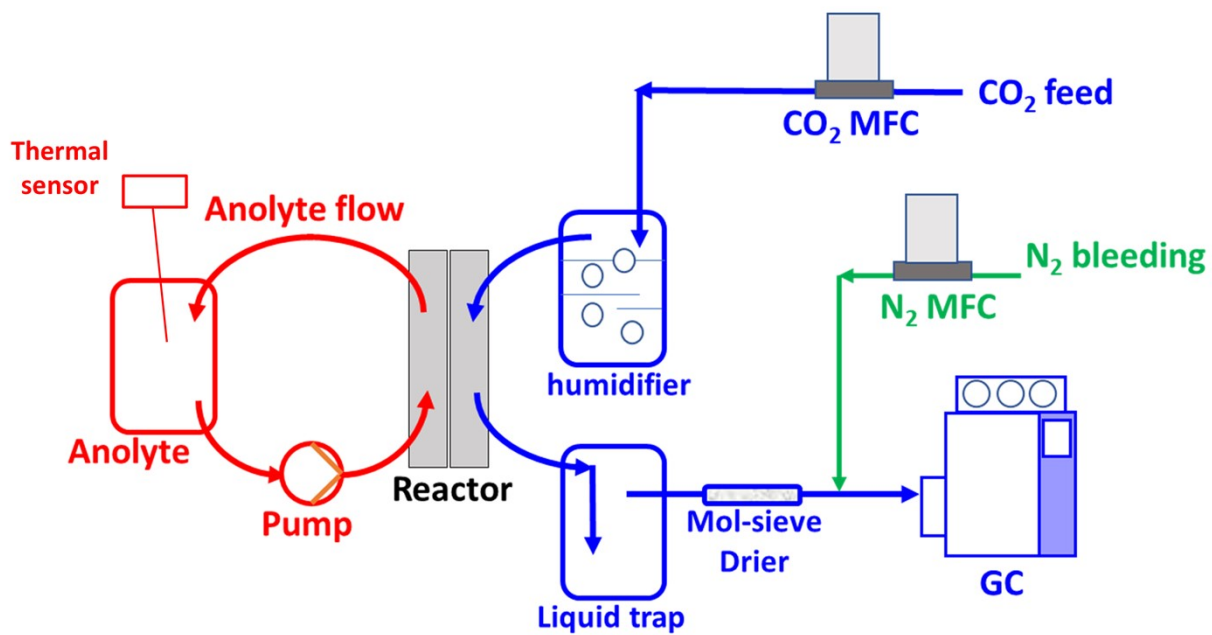
Supplementary Figure 11: **NiFe-LDH@NF anode after 200 h electrolysis.** Morphology change, new layer with cracks on top of the foam.



Supplementary Figure 12: **Anode serpentine flow field covered with particles.**



Supplementary Figure 13: **Back side of the Anode with an unchanged foam texture.**



Supplementary Figure 14: Test station.

5. Literature

1. Takano I, Isobe S, Sasaki TA, Baba Y. Nitrogenation of various transition metals by N²⁺-ion implantation. *Applied Surface Science*. 1989;37(1):25-32.
2. Petraki F, Papaefthimiou V, Kennou S. The electronic structure of Ni-phthalocyanine/metal interfaces studied by X-ray and ultraviolet photoelectron spectroscopy. *Organic Electronics*. 2007;8(5):522-8.
3. Dongol M, El-Denglawey A, Elhady AF, Abuelwafa AA. Structural properties of nano 5, 10, 15, 20-Tetraphenyl-21H,23H-porphine nickel (II) thin films. *Current Applied Physics*. 2012;12(5):1334-9.
4. Bondarchuk O, Morel A, Bélanger D, Goikolea E, Brousse T, Mysyk R. Thin films of pure vanadium nitride: Evidence for anomalous non-faradaic capacitance. *Journal of Power Sources*. 2016;324:439-46.
5. Luo Q, Lu C, Liu L, Zhu M. A review on the synthesis of transition metal nitride nanostructures and their energy related applications. *Green Energy & Environment*. 2023;8(2):406-37.
6. Baloch M, Shanmukaraj D, Bondarchuk O, Bekaert E, Rojo T, Armand M. Variations on Li₃N protective coating using ex-situ and in-situ techniques for Li^o in sulphur batteries. *Energy Storage Materials*. 2017;9:141-9.
7. Ningthoujam RS, Gajbhiye NS. Synthesis, electron transport properties of transition metal nitrides and applications. *Progress in Materials Science*. 2015;70:50-154.
8. Leineweber A, Jacobs H, Hull S. Ordering of nitrogen in nickel nitride Ni₃N determined by neutron diffraction. *Inorg Chem*. 2001;40(23):5818-22.
9. Biesinger MC, Lau LW, Gerson AR, Smart RS. The role of the Auger parameter in XPS studies of nickel metal, halides and oxides. *Phys Chem Chem Phys*. 2012;14(7):2434-42.
10. Li M, Lees EW, Ju W, Subramanian S, Yang K, Bui JC, et al. Local ionic transport enables selective PGM-free bipolar membrane electrode assembly. *Nat Commun*. 2024;15(1):8222.
11. Yan Z, Hitt JL, Zeng Z, Hickner MA, Mallouk TE. Improving the efficiency of CO₂ electrolysis by using a bipolar membrane with a weak-acid cation exchange layer. *Nat Chem*. 2021;13(1):33-40.
12. Yang K, Li M, Subramanian S, Blommaert MA, Smith WA, Burdyny T. Cation-Driven Increases of CO₂ Utilization in a Bipolar Membrane Electrode Assembly for CO₂ Electrolysis. *ACS Energy Lett*. 2021;6(12):4291-8.
13. Blommaert MA, Subramanian S, Yang K, Smith WA, Vermaas DA. High Indirect Energy Consumption in AEM-Based CO₂ Electrolyzers Demonstrates the Potential of Bipolar Membranes. *ACS Appl Mater Interfaces*. 2022;14(1):557-63.
14. Weekes DM, Salvatore DA, Reyes A, Huang A, Berlinguette CP. Electrolytic CO₂ Reduction in a Flow Cell. *Acc Chem Res*. 2018;51(4):910-8.
15. Kwen J, Schmidt TJ, Herranz J. Impact of Cathode Components' Configuration on the Performance of Forward-Bias Bipolar Membrane CO₂-Electrolyzers. *ACS Applied Energy Materials*. 2025;8(7):4152-65.

16. Siritanaratkul B, Khan MD, Yu EH, Cowan AJ. Alkali metal cations enhance CO(2) reduction by a Co molecular complex in a bipolar membrane electrolyzer. *Philos Trans A Math Phys Eng Sci.* 2024;382(2282):20230268.